Hyperspectral Image Denoising With Total Variation Regularization and Nonlocal Low-Rank Tensor Decomposition

Hongyan Zhang, *Senior Member, IEEE*, Lu Liu, Wei He, *Member, IEEE*, and Liangpei Zhang, *Fellow, IEEE*

***Abstract*— Hyperspectral images (HSIs) are normally corrupted by a mixture of various noise types, which degrades the quality of the acquired image and limits the subsequent application. In this article, we propose a novel denoising method for the HSI restoration task by combining nonlocal low-rank tensor decomposition and total variation regularization, which we refer to as TV-NLRTD. To simultaneously capture the nonlocal similarity and high spectral correlation, the HSI is first segmented into overlapping 3-D cubes that are grouped into several clusters by the k-means++ algorithm and exploited by low-rank tensor approximation. Spatial–spectral total variation (SSTV) regularization is then investigated to restore the clean HSI from the denoised overlapping cubes. Meanwhile, the ℓ_1-norm facilitates the separation of the clean nonlocal low-rank tensor groups and the sparse noise. The proposed TV-NLRTD method is optimized by employing the efficient alternating direction method of multipliers (ADMM) algorithm. The experimental results obtained with both simulated and real hyperspectral data sets confirm the validity and superiority of the proposed method compared with the current state-of-the-art HSI denoising algorithms.**

***Index Terms*— Denoising, Hyperspectral image (HSI), nonlocal low-rank, spatial–spectral total variation (SSTV), tensor decomposition.**

I. Introduction

A HYPERSPECTRAL image (HSI) is a high-dimensional data cube containing an array of 2-D gray images over hundreds of adjacent spectral bands. The abundant spectral information of HSIs is used in many applications, such as food safety [1], precision agriculture [2], mineral detection [3], and military reconnaissance [4]. Unfortunately, HSIs are normally corrupted by several types of noise, such as the Gaussian noise, stripes, dead pixels, and impulse noise. The generation of noise is derived from many aspects, including sensor noise (including photon (shot) noise, dark noise, and readout noise) and the atmospheric effect [7], [27]. The existence of noise not only degrades the image quality but also restricts the precision of the subsequent applications. In fact, the denoising results directly determine the performance of the related applications. Therefore, denoising of hyperspectral remote sensing images has important academic significance and application value.

Over the past few years, HSI denoising has attracted the attention of many scholars. From the perspective of the spatial domain, an HSI is equivalent to a gray image with many overlapping bands. Therefore, the most intuitive approach is to regard each band of the HSI as an independent gray image. Thus, the traditional gray image denoising methods, such as wavelet-based methods [6], the K-SVD algorithm [8], block-matching 3-D (BM3D) filtering [9], and total variation (TV) regularization [49], can be adopted to restore HSIs. However, such methods neglect the correlations between the different spectral bands, resulting in a poor performance in many cases. To take full advantage of the strong spectral correlation in HSIs, several spectral domain-based methods have been proposed. By assuming that the high-dimensional HSI underlies a low-dimensional intrinsic space, principal component analysis (PCA) [57] transforms the HSI into a lower dimensional linear space by orthogonal projection, and the restored HSI can then be obtained via inverse transformation of the first few principal component images that are regarded as containing most of the information. In [49], by adopting the strong assumption of piecewise smoothness, a cubic TV (CTV) model for HSI denoising was proposed. By considering the HSI as a 3-D tensor with multilinear algebra tools, the multidimensional Wiener filter (MWF) method utilizes the Wiener filtering to denoise the HSI after performing Tucker decomposition on the hyperspectral data [10], [11], [37], [38], [48], [55]. Nevertheless, these methods only focus on the additive white Gaussian noise, resulting in a less competitive performance for other types of mixed noise.

In reality, the actual noise in HSIs is much more complex than the Gaussian noise. In addition to the Gaussian noise, HSIs are usually corrupted by stripes, dead pixels or lines, impulse noise, and so on [27]. Inspiringly, many researchers have attempted to remove the mixed noise in HSIs [27], [31], [51]. Motivated by the robust PCA (RPCA) method [17], Zhang *et al.* [27] proposed the low-rank matrix recovery (LRMR) model by exploring the low-rank property of the 2-D form of hyperspectral imagery and considered the non-Gaussian noise as a sparse part. Although the LRMR method

Manuscript received April 20, 2019; revised September 4, 2019; accepted October 2, 2019. Date of publication November 8, 2019; date of current version April 22, 2020. This work was supported in part by the National Key Research and Development Program of China under Grant 2018YFB0504500 and in part by the National Natural Science Foundation of China under Grant 61871298 and Grant 41571362. *(Corresponding author: Wei He.)*

H. Zhang, L. Liu, and L. Zhang are with the State Key Laboratory of Information Engineering in Surveying, Mapping, and Remote Sensing, Wuhan University, Wuhan 430072, China (e-mail: zhanghongyan@whu.edu.cn; liuweilu@whu.edu.cn; zlp62@whu.edu.cn).

W. He is with the RIKEN Center for Advanced Intelligence Project, Geoinformatics Unit, Tokyo 130-0027, Japan (e-mail: wei.he@riken.jp).

Color versions of one or more of the figures in this article are available online at http://ieeexplore.ieee.org.

Digital Object Identifier 10.1109/TGRS.2019.2947333

has achieved competitive performances, it only utilizes the spectral information and causes some spatial distortion in the case of heavy noise. To further combine the spatial structure and spectral information of HSIs, He *et al.* [31] incorporated band-by-band TV regularization into the LRMR framework to capture the piecewise smoothness of the clean image from the spatial perspective, thus enhancing the denoising performance. However, such a bandwise TV regularization ignores the piecewise smoothness in the spectral domain, resulting in excessive smoothing of the restored image [13], [15], [24], [30]. Although some encouraging progress has been made, developing a denoising model for mixed noise by mining both spatial and spectral information has been less successful and still requires further research.

Nonlocal self-similarity has shown great potential in natural image denoising [14], [16], [19]. It characterizes the "homologous aggregation of microstructures" [12], which can be used to preserve edges and details. Consequently, the nonlocal self-similarity-based method has been successfully applied to HSIs for the Gaussian denoising. Xue and Zhao [59] combined rank-1 tensor decomposition with nonlocal low-rank regularization (NLR-R1TD) for HSI denoising to avoid the rank uncertainty. By integrating the multidimensional nonlocal means filter algorithm with a variational framework, Li *et al.* [43] proposed multidimensional nonlocal TV (MNLTV) for HSI denoising. Peng *et al.* [47] constructed a nonlocal tensor dictionary learning (TDL) model by explicitly considering the spatial and spectral self-similarity of multispectral imagery with a group-block-sparsity constraint. Xie *et al.* [50] provided a new multispectral image denoising model (ITSReg) with a designed sparsity measure under Tucker and canonical polyadic (CP) decomposition for tensors formed by nonlocal similar patches. In [58], an HSI denoising algorithm based on nonnegative Tucker decomposition was proposed to exploit the nonlocal similarity across the HSI cube. Despite their considerable advantages, these nonlocal-based methods ignore the problem of the complicated noise in HSIs, leading to unsatisfactory restoration results in real-world situations under a heavy mixed-noise scenario.

In this article, we build a bridge between nonlocal similarity and mixed-noise removal and propose the spatial–spectral total-variation-regularized nonlocal low-rank tensor decomposition (TV-NLRTD) method for HSI denoising. We consider that HSIs are usually corrupted by a combination of various types of noise, including the Gaussian noise, plus impulse noise, stripes, and deadlines, which are modeled as the sparse noise [25], [27], [28], [41], [45]. Fig. 1 shows the overall framework of the proposed model. As with our previous model [27], the noisy HSI is divided into the clean image, the Gaussian noise, and sparse noise. However, differing from the previous work, where it was assumed that the clean HSI should underlie a low-dimensional subspace, we exploit the nonlocal similarity of the clean HSI. To boost the performance, we also adopt the assumption that the restored HSI from the recovered nonlocal patches demonstrates a piecewise smooth structure. In summary, the main contributions of this article include the following three aspects.

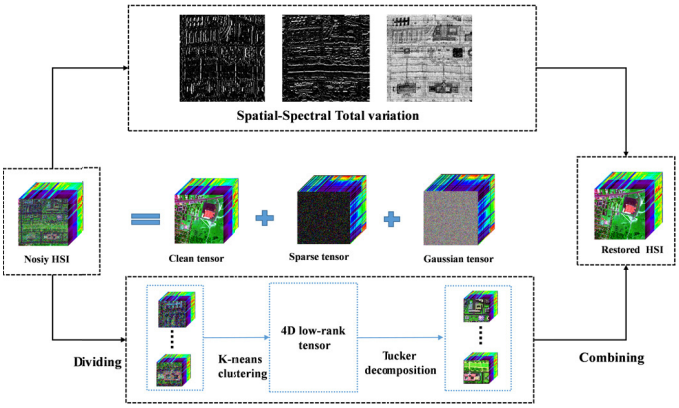

Fig. 1. Flowchart of the proposed TV-NLRTD method.

1) A nonlocal low-rank tensor decomposition model for HSI mixed-noise removal is proposed. Specifically, overlapping 3-D cubes extracted from the observed HSI are grouped into several clusters by the k-means++ algorithm [42]. Each cluster contains similar cubes, and hence, the nonlocal similarity between the spatial–spectral cubes is captured to exploit the structure of the clean image. The Tucker decomposition is then utilized to separate the clean cube from each clustered group, thus suppressing the mixed noise.
2) To further remove the mixed noise, spatial–spectral total variation (SSTV) regularization is integrated into the nonlocal low-rank tensor decomposition framework by exploiting the local piecewise smoothness of the clean image.
3) The alternating direction method of multipliers (ADMM) algorithm is employed to solve the proposed TV-NLRTD method. Both quantitative and visual evaluations of the experimental results obtained with simulated and real hyperspectral data sets confirm that the proposed method achieves better denoising results by simultaneously removing the mixed noise while preserving the image details.

The rest of this article is organized as follows. Some tensor-related notations and preliminaries are presented in Section II. Section III introduces the details of the proposed TV-NLRTD method, followed by the optimization solution of the ADMM algorithm. In Section IV, the results obtained in experiments undertaken with two simulated data sets and two real hyperspectral data sets are described to show the validity and practicability of the proposed method. Finally, Section V gives our conclusion and provides a discussion on future research.

II. Related Work

A. Notation and Preliminaries

In this article, we adopt the notation from [5] and denote a tensor as a Euler script letter, e.g., $\mathcal{A}$. A matrix is represented as a capitalized bold letter, e.g., $\mathcal{A}$. In addition, we denote variables as italic roman letters, e.g., a. For an N-mode tensor $\mathcal{A} \in \mathbb{R}^{I_1 \times \cdots I_n \times \cdots I_N}$, we denote its elements as $a_{i_1 \cdots i_n \cdots i_N}$, where $i_1 \leq i_n \leq i_N$. The mode-n flattening of a tensor means to take

the mode-n vectors of $\mathcal{A}$ as the columns and then convert this into a matrix, e.g., $\mathbf{A}_{(n)} \in \mathbb{R}^{I_n \times (I_1 \cdots I_{n-1} I_{n+1} \cdots I_N)}$.

The mode-n product of tensor $\mathcal{A} \in \mathbb{R}^{I_1 \times \cdots I_n \times \cdots I_N}$ by matrix $\mathbf{B} \in \mathbb{R}^{J_N \times I_N}$ is denoted by $\mathcal{C} = \mathcal{A} \times_n \mathbf{B}$, where $\mathcal{C} \in \mathbb{R}^{I_1 \times \cdots J_n \times \cdots I_N}$ is an Nth order tensor, and its entries are computed by $c_{i_1 \cdots i_{n-1} j_n i_{n+1} \cdots i_N} = \sum_{i_n} a_{i_1 \cdots i_{n-1} i_n i_{n+1} \cdots i_N} b_{j_n j_n}$. The n-rank of $\mathcal{A}$, denoted as r_n, can be seen as the dimension of the space formed by the tensor on each mode. The Frobenius norm of a tensor $\mathcal{A}$ is defined as $\|\mathcal{A}\|_F = (\sum_{i_1,\ldots,i_N} |a_{i_1,\ldots,i_N}|^2)^{1/2}$, and the ℓ_1-norm is calculated as $\|\mathcal{A}\|_1 = \sum_{i_1,\ldots,i_N} |a_{i_1,\ldots,i_N}|$.

B. Nonlocal Similarity Patch Matching

The nonlocal similarity of an HSI describes the fact that for each 3-D block of the HSI, there are many similar blocks in the nearby space. Typically, to exploit the self-similarity of the pattern structure in the image, the HSI is first segmented into overlapping 3-D blocks [47], and then, the nonlocal patch sets can be constructed by the k-means++ [42] clustering algorithm. In this way, the nonlocal procedure simultaneously exploits the spectral and spatial low-rank property of the HSI. For an n-order tensor, it can be decomposed into n factor matrices and one core tensor by the Tucker decomposition. The factor matrix on each mode is called the base matrix of the tensor or the principal component. Consequently, the Tucker decomposition can also be considered as high-order PCA [33]–[36] and can be used to depict the low-rank tensor approximation. The equation for the Tucker decomposition is formulated as

$$\mathcal{X} = \mathcal{G} \times_1 \mathbf{U}_1 \times_2 \mathbf{U}_2 \times \cdots \times_N \mathbf{U}_N \tag{1}$$

where $\mathcal{G}$ is the core tensor controlling the interaction between the factor matrices $\mathbf{U}_1 \in \mathbb{R}^{I_1 \times r_1}, \mathbf{U}_2 \in \mathbb{R}^{I_2 \times r_2}, \ldots, \mathbf{U}_N \in \mathbb{R}^{I_N \times r_N}$.

For the complex mixed noise in HSIs, different types of noise have very different properties, e.g., stripe noise is a special kind of noise with a certain periodicity, directionality, and distribution in the image [23]. This means that the statistical distribution of sparse noise is totally different from the Gaussian distribution of the Gaussian noise. However, the traditional nonlocal similar patch grouping methods are based on the Gaussian distribution assumption and adopt the ℓ_2-norm to characterize the patch similarity. These methods cannot be applied to the complex non-Gaussian noise, inspiring us to model the sparse noise and utilize more prior information for the restoration of the clean HSI.

C. TV Regularization

HSIs also demonstrate a strong piecewise smooth structure, and the related TV methods have been widely used in HSI processing [18], [20], [22], [23], [60]. Fig. 2 depicts the piecewise smooth property from both the spatial and spectral modes of HSIs. The TV norms can be divided into isotropic TV norms and anisotropic TV norms [44]. Although these two kinds of TV norm are both generated by discrete transform gradients, the isotropic model may cause obvious blurring artifacts for HSI noise removal [23], which inspires us to exploit the anisotropic TV norm in our model. For an HSI$\mathcal{X}$, the anisotropic SSTV norm can be described as

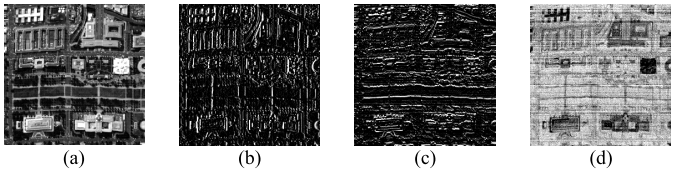

Fig. 2. Gradient images of the HSI cube in three different directions. (a) Original image. (b) Gradient image from the spatial horizontal direction. (c) Gradient image from the spatial vertical direction. (d) Gradient image from the spectral direction.

$$\|\mathcal{X}\|_{\text{SSTV}} = \|\mathbf{D}\mathcal{X}\|_1 = \|\mathbf{D}_h\mathcal{X}\|_1 + \|\mathbf{D}_v\mathcal{X}\|_1 + \|\mathbf{D}_s\mathcal{X}\|_1 \tag{2}$$

where $\mathbf{D}_h, \mathbf{D}_v, \mathbf{D}_s \in \mathbb{R}^{n_l \times n_c \times n_b}$ denotes the first-order forward finite-difference operators along the spatial horizontal, spatial vertical, and spectral directions, respectively. For the pixel at the spatial location (i, j) and the k_{th} spectral band $\mathcal{X}(i, j, k)$, each operator is defined as follows:

$$\begin{aligned} \mathbf{D}_h\mathcal{X} &= \mathcal{X}(i, j+1, k) - \mathcal{X}(i, j, k) \\ \mathbf{D}_v\mathcal{X} &= \mathcal{X}(i+1, j, k) - \mathcal{X}(i, j, k) \\ \mathbf{D}_s\mathcal{X} &= \mathcal{X}(i, j, k+1) - \mathcal{X}(i, j, k). \end{aligned} \tag{3}$$

III. SSTV-Regularized Nonlocal Low-Rank Tensor Decomposition for HSI Denoising

A. Problem Formulation

In the real world, HSIs are usually corrupted by various types of noise during the acquisition and transmission, such as the Gaussian noise, impulse noise, stripes, and dead pixels or lines. For an observed HSI $\mathcal{Y} \in \mathbb{R}^{n_l \times n_c \times n_b}$, n_b represents the number of spectral bands, and n_l, n_c are the width and height of the image, respectively. The mixed noise in hyperspectral remote sensing images can be divided into two parts according to the noise density distribution: the Gaussian noise and the sparse noise, where the sparse noise includes stripes, dead pixels or lines, and impulse noise [27]–[29]. To account for this, the noise degradation model of an HSI can be expressed as

$$\mathcal{Y} = \mathcal{X} + \mathcal{N} + \mathcal{S} \tag{4}$$

where $\mathcal{X} \in \mathbb{R}^{n_l \times n_c \times n_b}$ represents a clean HSI cube. $\mathcal{N} \in \mathbb{R}^{n_l \times n_c \times n_b}$ and $\mathcal{S} \in \mathbb{R}^{n_l \times n_c \times n_b}$ are the Gaussian noise and sparse noise, respectively. The final aim of HSI denoising is to recover $\mathcal{X}$ from $\mathcal{Y}$.

B. Proposed TV-NLRTD Model

In this section, we first introduce the nonlocal low-rank tensor decomposition (NLRTD) model and then present the proposed TV-NLRTD.

Since the clean HSI is high-dimensional data with a low-dimensional structure, the low-rank-based HSI mixed-noise removal methods have achieved good performances by exploiting this type of prior information [18], [31], [51]. However, the traditional low-rank-based HSI mixed-noise removal methods are based on either a local low-rank prior or a global low-rank regularization, which ignores the nonlocal self-similarity

of the hyperspectral remote sensing image. Inspiringly, with the consideration of the great success achieved by the nonlocal self-similarity in natural image [14], [16], [19], [56] and HSI [43], [47], [50], [58] denoising, we propose a nonlocal low-rank tensor model for HSI mixed-noise removal. Under the image degradation model (4), we explore the nonlocal similarity of the clean image $\mathcal{X}$ and propose an NLRTD method. The proposed method can be formulated as

$$\min \frac{1}{2}\|\mathcal{Y}-\mathcal{X}-\mathcal{S}\|_F^2+\lambda_2\|\mathcal{S}\|_1+\lambda_3\|\mathcal{X}\|_{NL}. \tag{5}$$

The last item is the nonlocal low-rank regularizer, for which the nonlocal low-rank approximation $\|\mathcal{X}\|_{NL}$ is described as follows. First, the clean image $\mathcal{X}$ is segmented into many overlapping 3-D blocks of size $w\times w\times n_b$ to build a 3-D patch set $S: S=\{\mathcal{P}_{i,j}\in\mathbb{R}^{w\times w\times n_b}\}_{1\le i\le n_l-w+1,1\le j\le n_c-w+1}$. By clustering the patch set S into K clusters with the k-means++ algorithm [42], the constructed fourth-order tensor with the size $w\times w\times n_b\times N_p$ is formed by a group of nonlocal similar cubes, where N_p is the number of nonlocal similar patches in the p_{th} cluster. We denote $\mathbf{R}p\mathcal{X}$ as the constructed fourth-order tensor for the p_{th} cluster. Since each cluster has a low-rank structure from nonlocal and spectral perspectives, $\mathbf{R}p\mathcal{X}$ can then be ideally approximated by a low-rank tensor $\mathcal{L}_p$, i.e., $\mathbf{R}_p\mathcal{X}\approx\mathcal{L}_p$. Thus, the nonlocal regularization can be formulated as

$$\|\mathcal{X}\|_{NL}=\sum_{\text{p=1}}^{K}\|\mathbf{R}_p(\mathcal{X})-\mathcal{L}_p\|_F^2. \tag{6}$$

By summing all the clusters with an averaging operator, the nonlocal low-rank approximation term $\mathcal{X}_{NL}$ can be easily derived as

$$\mathcal{X}_{\text{NL}}=\left(\sum_p\mathbf{R}_p^T\mathbf{R}_p\right)^{-1}\sum_p\mathbf{R}_p^T\mathcal{L}_p. \tag{7}$$

Since $\mathcal{L}_p$ is a low-rank tensor, it can be modeled by the Tucker decomposition as follows:

$$\mathcal{L}_p=\mathcal{G}_p\times_1\mathbf{U}_{1p}\times_2\mathbf{U}_{2p}\times_3\mathbf{U}_{3p}\times_4\mathbf{U}_{4p} \tag{8}$$

where $\mathcal{G}_p$ is the core tensor, and $\mathbf{U}_{1p},\mathbf{U}_{2p},\mathbf{U}_{3p},\mathbf{U}_{4p}$ are factor matrices with orthogonal columns. Thus, the NLRTD model for mixed-noise denoising can be formulated as

$$\begin{aligned}\min_{\mathcal{X},\mathcal{S},\mathcal{G}_p,\mathbf{U}_{ip}}\ &\frac{1}{2}\|\mathcal{Y}-\mathcal{X}-\mathcal{S}\|_F+\lambda_2\|\mathcal{S}\|_1+\lambda_3\\&\times\sum_p\|\mathbf{R}_p\mathcal{X}-\mathcal{G}_p\times_1\mathbf{U}_{1p}\times_2\mathbf{U}_{2p}\times_3\mathbf{U}_{3p}\times_4\mathbf{U}_{4p}\|_F^2\\&\text{s.t. }\mathbf{U}_{ip}^T\mathbf{U}_{ip}=\mathbf{I},\quad(i=1,2,3,4)\end{aligned} \tag{9}$$

where λ_2, λ_3 are the regularization parameters. The nonlocal low-rank regularizer is an extension of the global low-rank regularizer described as $\|\mathcal{X}-\mathcal{G}\times_1\mathbf{U}_1\times_2\mathbf{U}_2\times_3\mathbf{U}_3\times_4\mathbf{U}_4\|_F^2$. However, compared to the global low-rank regularizer, the nonlocal low-rank regularizer has the ability to simultaneously capture the spatial self-similarity and spectral correlation by adopting low-rank tensor approximation to process each nonlocal similarity group tensor. Thus, the proposed model has the ability to boost the denoising performance. Stripes and other kinds of noise such as impulse noise and dead pixels or lines only occupy a very small proportion in the whole image. Accordingly, this noise part can be regarded as the sparse noise $\|\mathcal{S}\|_1$ and regularized by the ℓ_1-norm [26]. Adding a sparse part is more conducive to maintaining the texture details of the image. Unlike the previous nonlocal-based approaches, the proposed method considers not only the nonlocal low-rank prior but also the global piecewise smoothness across the clean HSI, thus boosting the denoising performance.

The nonlocal low-rank regularizer segments the image $\mathcal{X}$ into cubes, denoises each cube group separately, and finally merges the denoised patches into the whole image. However, this procedure ignores the global smoothness of the image $\mathcal{X}$. Inspiringly, we integrate both the nonlocal low-rank tensor decomposition and the SSTV model to simultaneously explore the global smoothness, nonlocal similarity, and spectral low-rank property for HSI denoising. We denote $\mathbf{D}=[\mathbf{D}_h^T,\mathbf{D}_v^T,\mathbf{D}_s^T]^T$ as the concatenation of the three TV operations. The proposed TV-NLRTD method is then formulated as

$$\begin{aligned}\min_{\mathcal{X},\mathcal{S},\mathcal{G}_p,\mathbf{U}_{ip}}\ &\frac{1}{2}\|\mathcal{Y}-\mathcal{X}-\mathcal{S}\|_F^2+\lambda_1\|\mathbf{D}\mathcal{X}\|_1+\lambda_2\|\mathcal{S}\|_1+\lambda_3\\&\times\sum_p\|\mathbf{R}_p\mathcal{X}-\mathcal{G}_p\times_1\mathbf{U}_{1p}\times_2\mathbf{U}_{2p}\times_3\mathbf{U}_{3p}\times_4\mathbf{U}_{4p}\|_F^2\\&\text{s.t. }\mathbf{U}_{ip}^T\mathbf{U}_{ip}=\mathbf{I},\quad(i=1,2,3,4).\end{aligned} \tag{10}$$

Such integrative consideration exploits the inherent spectral and spatial correlation in the clean HSI and the complexity of the noise, thus helps in the separation of mixed noise and the preservation of edge information. It is clear that the proposed model (10) is a nonconvex optimization problem due to the nonconvexity of the Tucker decomposition. To solve the equation optimization, we employ the ADMM [32], [59] algorithm, dividing the complex optimization (10) into several simple subproblems [56]. Specifically, the nonconvex optimization of the Tucker decomposition can be efficiently solved by the higher order orthogonal iteration (HOOI) algorithm [5]. Although the theoretical convergence is not guaranteed, we present the convergence of the objective values via the experiments. More details of the algorithm are presented in Section III-C.

C. Optimization Algorithms

For efficiency, the variable splitting method [21] is employed to solve the proposed model. The TV-NLRTD method can be converted into an equality-constrained problem by introducing the augmented variables $\mathcal{F}$ and $\mathcal{Z}$

$$\begin{aligned}\min_{\mathcal{X},\mathcal{F},\mathcal{Z},\mathcal{S},\mathcal{G}_p,\mathbf{U}_{ip}}\ &\frac{1}{2}\|\mathcal{Y}-\mathcal{X}-\mathcal{S}\|_F^2+\lambda_1\|\mathcal{F}\|_1+\lambda_2\|\mathcal{S}\|_1+\lambda_3\\&\times\sum_p\|\mathbf{R}_p\mathcal{X}-\mathcal{G}_p\times_1\mathbf{U}_{1p}\times_2\mathbf{U}_{2p}\\&\times_3\mathbf{U}_{3p}\times_4\mathbf{U}_{4p}\|_F^2\\&\text{s.t. }\mathbf{D}\mathcal{Z}=\mathcal{F},\mathcal{X}=\mathcal{Z},\mathbf{U}_{ip}^T\mathbf{U}_{ip}=\mathbf{I},\quad(i=1,2,3,4).\end{aligned} \tag{11}$$

Equation (11) can be optimized with the ADMM algorithm. The augmented Lagrangian function of (11) is as follows:

$$\begin{aligned} &L(\mathcal{X},\mathcal{S},\mathcal{F},\mathcal{Z},\mathcal{G}_p,\mathbf{U}_{ip},Q_1,Q_2)\\ &=\frac{1}{2}\|\mathcal{Y}-\mathcal{X}-\mathcal{S}\|_F^2+\lambda_1\|\mathcal{F}\|_1\\ &\quad+\frac{\mu}{2}\|\mathbf{D}\mathcal{Z}-\mathcal{F}-Q_1\|_F^2+\lambda_2\|\mathcal{S}\|_1+\frac{\mu}{2}\|\mathcal{X}-\mathcal{Z}-Q_2\|_F^2+\lambda_3\\ &\quad\times\sum_p\|\mathbf{R}_p\mathcal{X}-\mathcal{G}_p\times_1\mathbf{U}_{1p}\times_2\mathbf{U}_{2p}\times_3\mathbf{U}_{3p}\times_4\mathbf{U}_{4p}\|_F^2\\ &\text{s.t. }\mathbf{U}_{ip}^T\mathbf{U}_{ip}=\mathbf{I},\quad(i=1,2,3,4) \end{aligned}\tag{12}$$

where μ is the penalty parameter and Q_1, Q_2 are the Lagrange multipliers. Equation (12) can be decomposed into several subproblems for each variable, and the solution of the model can be established by iteratively optimizing the corresponding subfunctions.

1) Update $\mathcal{F}$: By fixing the other variables, the optimization function is

$$\mathcal{F}^{(k+1)}=\arg\min_{\mathcal{F}}\lambda_1\|\mathcal{F}\|_1+\frac{\mu}{2}\|\mathbf{D}\mathcal{Z}-\mathcal{F}-\mathcal{Q}_1\|_F^2.\tag{13}$$

With the introduction of the soft-thresholding operator

$$\text{Soft}(x,\lambda)=\begin{cases}x-\lambda, & \text{if } x>\lambda\\ x+\lambda, & \text{if } x<\lambda\\ 0, & \text{otherwise.}\end{cases}\tag{14}$$

We can then update $\mathcal{F}$ as

$$\mathcal{F}^{(k+1)}=\text{soft}(\mathbf{D}\mathcal{Z}-Q_1,\lambda_1/\mu).\tag{15}$$

2) Update $\mathcal{Z}$: While fixing the other variables, the optimization is equivalent to the following:

$$\begin{aligned}\mathcal{Z}^{(k+1)}=\arg\min_{\mathcal{Z}}\frac{\mu}{2}\|\mathbf{D}\mathcal{Z}-\mathcal{F}-Q_1\|_F^2\\ +\frac{\mu}{2}\|\mathcal{X}-\mathcal{Z}-Q_2\|_F^2.\end{aligned}\tag{16}$$

As can be seen, (16) is a convex quadratic optimization problem with the following closed-form solution:

$$\mathcal{Z}^{(k+1)}=(\mathbf{D}^T\mathbf{D}+\mathbf{I})^{-1}(\mathbf{D}^T\mathcal{F}+\mathbf{D}^TQ_1+\mathcal{X}-Q_2).\tag{17}$$

3) Update $\{\mathcal{G}_p,\mathbf{U}_{ip}\}$: While fixing the other variables

$$\begin{aligned}\{\mathcal{G}_p,\mathbf{U}_{ip}\}=\arg\min_{\mathcal{G},\mathbf{U}_i}\sum_p\|\mathbf{R}_p\mathcal{X}-\mathcal{G}_p\times_1\mathbf{U}_{1p}\times_2\mathbf{U}_{2p}\\ \times_3\mathbf{U}_{3p}\times_4\mathbf{U}_{4p}\|_F^2\\ \text{s.t. }\mathbf{U}_{ip}^T\mathbf{U}_{ip}=\mathbf{I}\quad(i=1,2,3,4).\end{aligned}\tag{18}$$

The classic HOOI algorithm [5] can be used to approximately solve the optimization problem (18) to obtain $\{\mathcal{G}_p,\mathbf{U}_{ip}\}$.

4) Update $\mathcal{X}$: While fixing the other variables, and by using (7), the optimization is equivalent to

$$\begin{aligned}\mathcal{X}^{(k+1)}=\arg\min_{\mathcal{X}}\frac{1}{2}\|\mathcal{Y}-\mathcal{X}-\mathcal{S}\|_F^2+\frac{\mu}{2}\|\mathcal{X}-\mathcal{Z}-Q_2\|_F^2\\ +\lambda_3\times\sum_p\|\mathbf{R}_p\mathcal{X}-\mathcal{G}_p\times_1\mathbf{U}_{1p}\times_2\mathbf{U}_{2p}\\ \times_3\mathbf{U}_{3p}\times_4\mathbf{U}_{4p}\|_F^2.\end{aligned}\tag{19}$$

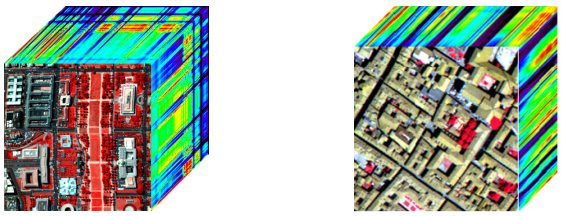

(a) (b)

Fig. 3. (a) HYDICE Washington DC Mall data set. (b) Pavia city center data set used in the simulated data experiments.

The solution of (19) is as follows:

$$\begin{aligned}&\mathcal{X}^{(k+1)}\\ &=\left(\mu\mathbf{I}+\mathbf{I}+\lambda_3\sum_{\text{p}}\mathbf{R}_p^T\mathbf{R}_p\right)^{-1}\\ &\quad\times\left(\mathcal{O}-\lambda_3\sum_{\text{p}}\mathbf{R}_p^T\mathcal{G}_p\times_1\mathbf{U}_{1p}\times_2\mathbf{U}_{2p}\times_3\mathbf{U}_{3p}\times_4\mathbf{U}_{4p}\right)\end{aligned}\tag{20}$$

where $\mathcal{O}=\mathcal{Y}-\mathcal{S}+\mu*(\mathcal{Z}+Q_2)$.

5) Update $\mathcal{S}$: While fixing the other variables

$$\mathcal{S}^{(k+1)}=\arg\min_{\mathcal{S}}\frac{1}{2}\|\mathcal{Y}-\mathcal{X}-\mathcal{S}\|_F^2+\lambda_2\|\mathcal{S}\|_1.\tag{21}$$

Equation (21) is also a soft-thresholding problem and has the solution

$$\mathcal{S}^{(k+1)}=\text{soft}(\mathcal{Y}-\mathcal{X},\lambda_2).\tag{22}$$

6) Update the Multipliers Q_1, Q_2:

$$\begin{aligned}Q_1^{(k+1)}&=Q_1^{(k)}-(\mathbf{D}\mathcal{Z}-\mathcal{F})\\ Q_2^{(k+1)}&=Q_2^{(k)}-(\mathcal{X}-\mathcal{Z}).\end{aligned}\tag{23}$$

The procedure of the proposed TV-NLRTD method is summarized in Algorithm 1. As can be seen, the inputs are as follows: the noisy HSI $\mathcal{Y}\in\mathrm{R}^{n_l\times n_c\times n_b}$, the block size $w\times w\times n_b$ for nonlocal searching, the stopping criterion ε, and the regularization parameters λ_1, λ_2, λ_3. For the experiment described in Section IV, the block size $w\times w\times n_b$ was set as $8\times 8\times n_b$, and the step size was set as $4\times 4\times n_b$. The stopping criterion ε was set to $1e-6$. We adopt the well-known AIC/MDL method to estimate the rank of each mode $\mathcal{L}_p$ [47]. The cluster number value is estimated via $n_l\times n_c/100$, as in [47]. At the beginning of the iteration, we initialize the variables $\mathcal{X}=\mathcal{Z}=\mathcal{S}=0$ and the multipliers $\mathcal{Q}_1=\mathcal{Q}_2=0$. The final output of Algorithm 1 is the restored HSI $\mathcal{X}\in\mathrm{R}^{n_l\times n_c\times n_b}$.

IV. Experimental Results and Discussion

In this section, we describe the experiments undertaken with both simulated and real data sets to verify the efficiency and practicability of the proposed method for HSI denoising. For comparison, six different HSI denoising methods were employed as benchmarks in the experiments, i.e., block-matching and 4-D filtering (BM4D) [46], TDL [47], LRMR [27], TV-regularized low-rank matrix factorization (LRTV) [31], TV-regularized low-rank constraint and SSTV (LSSTV) [40], and SSTV-regularized local

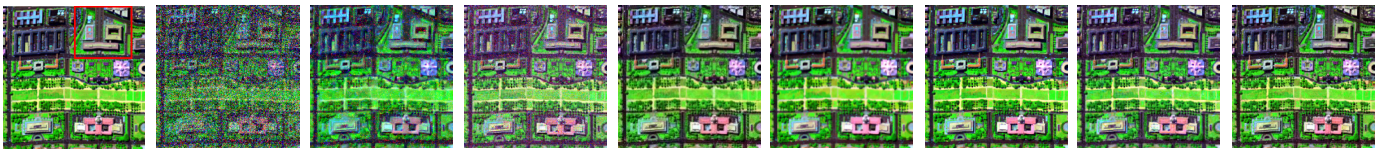

(a) (b) (c) (d) (e) (f) (g) (h) (i)

Fig. 4. Washington DC Mall image before and after denoising. (a) Original false-color image (R: 180, G: 61, B: 9). (b) Simulated noisy image in Case 2. The restored images of (c) BM4D, (d) TDL, (e) LRMR, (f) LRTV, (g) LSSTV, (h) LLRSSTV, and (i) TV-NLRTD.

(a) (b) (c) (d) (e) (f) (g) (h) (i)

Fig. 5. Pavia city center image before and after denoising. (a) Original image of band 51. (b) Simulated noisy image in Case 2. The restored images of (c) BM4D, (d) TDL, (e) LRMR, (f) LRTV, (g) LSSTV, (h) LLRSSTV, and (i) TV-NLRTD.

Algorithm 1 TV-NLRTD Algorithm

Input: The noisy HSI $\mathcal{Y} \in \mathrm{R}^{n_l \times n_c \times n_b}$, stopping criterion ε, block size $\mathrm{w} \times w \times n_b$, regularization parameters $\lambda_1, \lambda_2, \lambda_3$

Output: The restored HSI $\mathcal{X} \in \mathrm{R}^{n_l \times n_c \times n_b}$

Initialize: $\mathcal{X} = \mathcal{Z} = \mathcal{S} = 0$, $\mathcal{Q}_1 = \mathcal{Q}_2 = 0$, $\mu = 10^2$, and $\mathrm{k} = 0$

Repeat until convergence

1. Update $\mathcal{F}$ via (16).
2. Update $\mathcal{Z}$ via (17).
3. Construct the non-local low-rank tensor (Section 3.2) and update $\{\mathcal{G}_p, \mathbf{U}_{ip}\}$ via (18), and update $\mathcal{X}$ via (19).
4. Update $\mathcal{S}$ via (22).
5. Update Q_1, Q_2 via (23).
6. Update the iterations: $k := k + 1$

Check the convergence conditions: $\frac{\|\mathcal{X}^{(k)} - \mathcal{X}^{(k+1)}\|_F^2}{\|\mathcal{Y}\|_F^2} \leq \varepsilon$

low-rank matrix recovery (LLRSSTV) [51]. Each band of the HSI was first normalized to the range [0, 1]. In the experiments, all the parameters of the comparison algorithms were fine-tuned, as described in their reference articles.

A. Simulated Data Experiments

Two public hyperspectral data sets—the Washington DC Mall data set and the Pavia city center data set—were employed in the simulated experiments. The Washington DC Mall data set (available at: https://engineering.purdue.edu/~biehl/MultiSpec/hyperspectral.html) was acquired by the hyperspectral digital imagery collection experiment (HYDICE) and has a size of 1208 × 307 × 191. A subimage of size 256 × 256 × 191 was selected in the experiment, as shown in Fig. 3(a). The Pavia city center data set was collected by the Reflective Optics System Imaging Spectrometer [61]. After removing some heavily noise-contaminated bands, a subimage of size 200 × 200 × 80 was used in the experiment, as presented in Fig. 3(b).

In the simulated experiments, several types of noise were added to the two HSI data sets as the following three cases:

Case 1: The same intensity of the Gaussian noise and impulse noise was added to each band. The percentage of the impulse noise was varied from 0.05 to 0.2. The variance of the Gaussian noise was increased from 0.025 to 0.1.

Case 2: Different intensity Gaussian noise and impulse noise were added for the different bands. The variance of the added Gaussian noise was randomly varied between 0 and 0.2, and the percentage of the impulse noise was randomly selected from 0 to 0.2 in the same way.

Case 3: Stripes were randomly added to 20% of the bands on the basis of Case 2. The numbers of stripes for each band were randomly selected from 20 to 40.

1) Visual Quality Comparison: Figs. 4–7 present the visual effects of the different denoising methods for the two simulated data sets in Case 2. The false-color composite images by bands 180, 61, and 9 of the Washington DC Mall data set and the simulated noisy image are presented in Fig. 4(a) and (b), respectively. The original band 51 of the Pavia city center data set and the simulated noisy image is displayed in Fig. 5(a) and (b), respectively. Figs. 4(c)–(i) and 5(c)–(i) display the denoising results of the different methods. In order to observe the local detail, magnified results of parts of Figs. 4 and 5 are shown in Figs. 6 and 7, respectively. According to Figs. 6 and 7, it is clear that BM4D and TDL cannot remove the heavy Gaussian noise and impulse noise. LRMR eliminates more mixed noise than these three methods but still leaves small amounts of residual noise. It can be seen that LRTV, LSSTV, and LLRSSTV obtain better visual performances; however, they both smooth the image details to a certain degree, e.g., the building edge information is blurred. In the meantime, it is clear that the proposed TV-NLRTD method achieves the best visual performance in obtaining a clean image and retaining the essential edge structures. This is mainly because the TV-NLRTD method effectively combines the nonlocal and local information from both the spectral and spatial perspectives.

For a more intuitive comparison of the different recovery performances, Figs. 8 and 9 present the spectral signatures of typical features of the two simulated data sets. Fig. 8 shows the spectrum of the pixel (86, 160) from the Washington DC Mall image, before and after restoration in simulated Case 2, in which this pixel represents the "Grasslands" class. Fig. 9 displays the spectrum of the pixel (145, 110) from the Pavia city center image, before and after restoration in simulated

(a) (b) (c) (d) (e) (f) (g) (h) (i)

Fig. 6. Magnified results from Fig. 4. (a) Original false-color image (R: 180, G: 61, and B: 9). (b) Noisy image. The restored image of (c) BM4D, (d) TDL, (e) LRMR, (f) LRTV, (g) LSSTV, (h) LLRSSTV, and (i) TV_NLRTD.

(a) (b) (c) (d) (e) (f) (g) (h) (i)

Fig. 7. Magnified results from Fig. 5. (a) Original image of band 51. (b) Noisy image. The restored images of (c) BM4D, (d) TDL, (e) LRMR, (f) LRTV, (g) LSSTV, (h) LLRSSTV, and (i) TV-NLRTD.

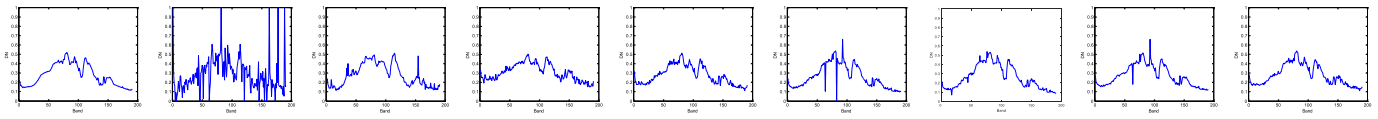

(a) (b) (c) (d) (e) (f) (g) (h) (i)

Fig. 8. Spectrum of the pixel (86, 160) from the Washington DC Mall image before and after restoration in Case 2. (a) Original. (b) Noisy. (c) BM4D. (d) TDL. (e) LRMR. (f) LRTV. (g) LSSTV. (h) LLRSSTV. (i) TV-NLRTD.

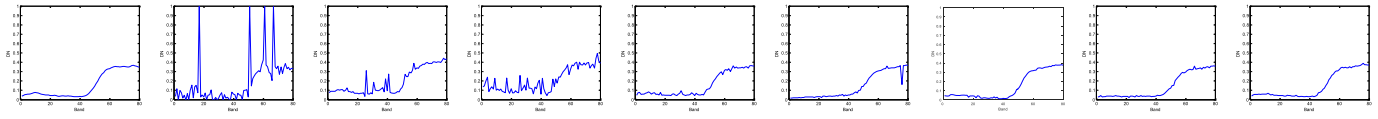

(a) (b) (c) (d) (e) (f) (g) (h) (i)

Fig. 9. Spectrum of the pixel (145, 110) from the Pavia city center image before and after restoration in Case 2. (a) Original. (b) Noisy. (c) BM4D. (d) TDL. (e) LRMR. (f) LRTV. (g) LSSTV. (h) LLRSSTV. (i) TV-NLRTD.

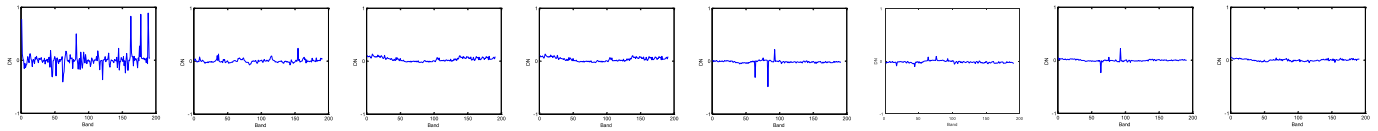

(a) (b) (c) (d) (e) (f) (g) (h)

Fig. 10. Difference between the spectrum of the noise-free pixel (86, 160) from the Washington DC Mall image before and after restoration in Case 2. (a) Noisy. (b) BM4D. (c) TDL. (d) LRMR. (e) LRTV. (f) LSSTV. (g) LLRSSTV. (h) TV-NLRTD.

Case 2, in which this pixel belongs to the "Building" class. From Figs. 8(c) and 9(c), it can be observed that the simulated noise causes evident jagged distortion in the spectral curves. Clearly, it can be seen that the spectral curves of the proposed TV-NLRTD method are much smoother than those of the other methods, for both data sets. Furthermore, the difference between the recovered spectral curves and the spectrum of the noise-free pixel (86, 160) from the Washington DC Mall image and pixel (145, 110) from the Pavia city center image is presented in Figs. 10 and 11, respectively. According to Figs. 10 and 11, it is clear that the proposed TV-NLRTD method shows the smallest difference with the clean pixel spectra, which proves that the denoising performance of the proposed method is better than that of the other benchmark methods, and it preserves the spectral information well.

Figs. 12 and 13 present the vertical profiles of some typical bands for the two simulated data sets in Case 2. Fig. 12 shows the vertical mean profiles of band 20 of the Washington DC Mall image before and after restoration. Fig. 13 displays the vertical profiles of band 31 of the Pavia city center image. The vertical axis represents the mean digital number (DN) value of each column, and the horizontal axis represents the column number of the HSI. From Figs. 12(b) and 13(b), it can be seen that rapid fluctuations occur due to the existence of the mixed noise. As shown in Figs. 12(c)–(i) and 13(c)–(i), it can be clearly observed that the proposed TV-NLRTD method produces the closest curves to the original HSI. It can, thus, be considered that the proposed method also retains the spatial information well.

2) Quantitative Comparison: To give a comprehensive quantitative evaluation of the denoising performance, the following evaluation indices are employed for the results of the simulated experiments: the peak signal-to-noise ratio (PSNR), the structural similarity (SSIM) index [52], the Erreur Relative Globale Adimensionnelle de Synthese (ERGAS) [53], and the spectral angle mapper (SAM) [54]. The values of PSNR and

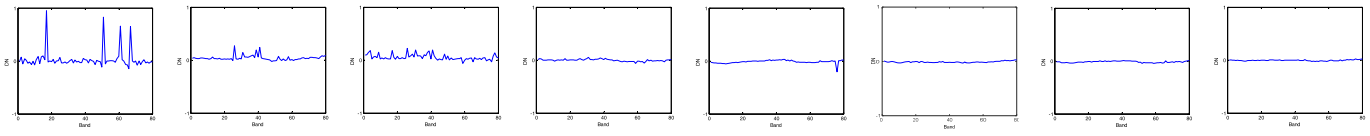

(a) (b) (c) (d) (e) (f) (g) (h)

Fig. 11. Difference between the spectrum of the noise-free pixel (145, 110) from the Pavia city center image before and after restoration in Case 2. (a) Noisy. (b) BM4D. (c) TDL. (d) LRMR. (e) LRTV. (f) LSSTV. (g) LLRSSTV. (h) TV-NLRTD.

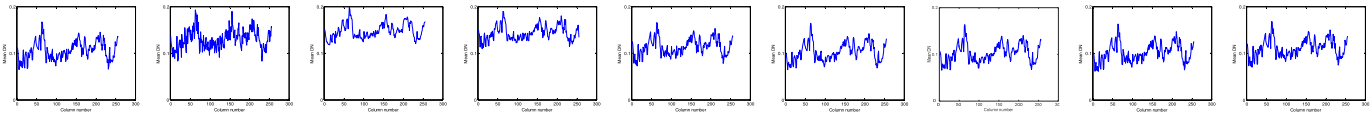

(a) (b) (c) (d) (e) (f) (g) (h) (i)

Fig. 12. Vertical profiles of band 20 of the Washington DC Mall image before and after restoration in Case 2. (a) Original. (b) Noisy. (c) BM4D. (d) TDL. (e) LRMR. (f) LRTV. (g) LSSTV. (h) LLRSSTV. (i) TV-NLRTD.

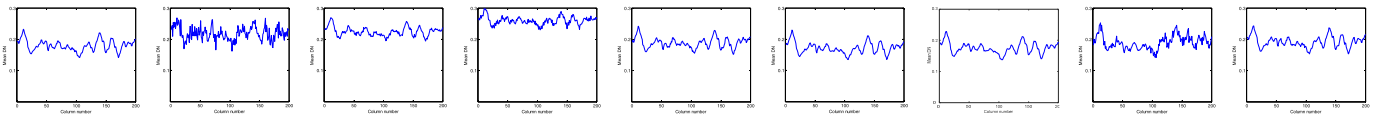

(a) (b) (c) (d) (e) (f) (g) (h) (i)

Fig. 13. Vertical profiles of band 31 of the Pavia city center image before and after restoration in Case 2. (a) Original. (b) Noisy. (c) BM4D. (d) TDL. (e) LRMR. (f) LRTV. (g) LSSTV. (h) LLRS-STV. (i) TV-NLRTD.

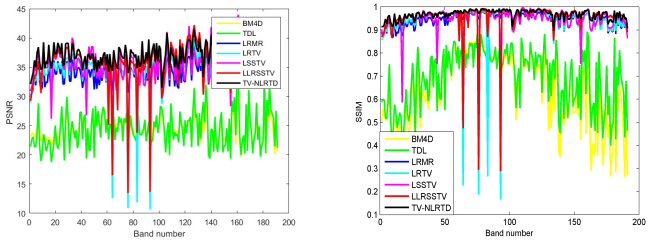

(a) (b)

Fig. 14. PSNR and SSIM values of each band in the experiment with the Washington DC Mall image in Case 2. (a) PSNR. (b) SSIM.

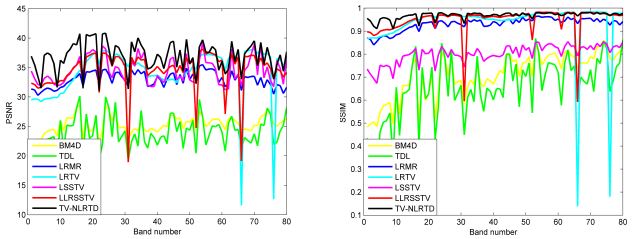

(a) (b)

Fig. 15. PSNR and SSIM values of each band in the experiment with the Pavia city center image in Case 2. (a) PSNR. (b) SSIM.

SSIM are proportional to the quality of the image, while the values of ERGAS and SAM are inversely proportional to the quality of the image.

The quantitative assessment results for the different denoising methods with the Washington DC Mall and Pavia city center data sets are shown in Tables I and II, respectively. The best results for each quality index are labeled in boldface,

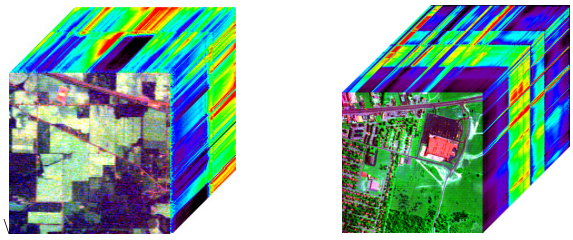

(a) (b)

Fig. 16. (a) AVIRIS Indian Pines data set used in the real data experiments. (b) HYDICE Urban data set used in real data experiments.

and the second-best results are underlined. It can be clearly observed that the proposed TV-NLRTD method outperforms all the other algorithms in almost all four quantitative indices. Meanwhile, it can be seen that with an increase in the intensity of the mixed noise, the superiority of the proposed algorithm becomes more obvious. In addition, Figs. 14 and 15 present the PSNR and SSIM values for each band in Case 2. From these results, it can be shown more intuitively that the proposed TV-NLRTD achieves the best denoising performance in almost all the bands on the two simulated data sets. This demonstrates that the proposed TV-NLRTD method can preserve the spatial and spectral structures of the original HSI to the greatest extent while effectively removing the mixed noise.

B. Real Data Experiments

We chose two real HSI data sets acquired by the NASA Airborne Visible/Infrared Imaging Spectrometer (AVIRIS) and HYDICE sensors to verify the effectiveness and practicability of the proposed method.

TABLE I
QUANTITATIVE EVALUATION RESULTS OF THE DIFFERENT DENOISING METHODS ON THE WASHINGTON DC MALL DATA SET

Noise case	Level	Evaluation index	Noise	BM4D	LRMR	TDL	LRTV	LSSTV	LLRSSTV	TV-NLRTD
Case 1	G=0.025 P=0.05	PSNR	17.10	26.42	42.24	31.72	41.20	42.28	44.26	**44.75**
		SSIM	0.451	0.817	0.989	0.932	0.987	0.989	0.992	**0.993**
		SAM	0.641	0.263	0.088	0.128	0.122	0.128	0.067	**0.063**
		ERGAS	602.54	197.98	37.12	115.51	86.33	115.51	29.36	**29.04**
	G=0.05 P=0.1	PSNR	13.80	23.98	37.74	26.55	38.40	38.34	39.58	**40.23**
		SSIM	0.231	0.623	0.970	0.839	0.964	0.975	0.980	**0.985**
		SAM	0.869	0.309	0.121	0.173	0.178	0.173	**0.106**	0.122
		ERGAS	962.58	282.35	59.31	200.95	126.69	200.95	48.85	**46.87**
	G=0.075 P=0.15	PSNR	11.99	23.51	34.85	24.36	35.50	35.81	36.18	**37.22**
		SSIM	0.144	0.681	0.946	0.783	0.941	0.957	0.959	**0.967**
		SAM	0.910	0.178	0.151	0.140	0.306	0.14	0.142	**0.133**
		ERGAS	1.83e+3	227.11	81.98	233.21	228.11	233.21	71.12	**63.95**
	G=0.1 P=0.2	PSNR	10.69	21.74	32.68	20.96	33.77	33.32	33.67	**35.05**
		SSIM	0.101	0.556	0.919	0.659	0.925	0.918	0.934	**0.949**
		SAM	0.929	0.255	0.172	0.251	0.361	0.251	0.176	**0.156**
		ERGAS	1.37e+3	352.05	105.01	391.64	181.29	391.64	93.96	**81.75**
Case 2	Gaussian + impulse	PSNR	14.33	24.30	34.26	24.37	34.45	35.75	36.42	**37.27**
		SSIM	0.253	0.638	0.942	0.688	0.934	0.944	0.956	**0.966**
		SAM	0.776	0.275	0.127	0.270	0.247	0.27	0.190	**0.134**
		ERGAS	899.31	278.60	84.36	291.62	135.00	291.62	95.35	**66.52**
Case 3	Gaussian +stripes+ impulse	PSNR	14.23	24.23	34.02	24.39	34.37	35.52	36.39	**36.75**
		SSIM	0.247	0.635	0.940	0.696	0.932	0.939	0.955	**0.960**
		SAM	0.778	0.275	0.192	0.267	0.246	0.267	0.196	**0.152**
		ERGAS	903.97	279.03	86.61	289.09	134.49	289.09	96.35	**75.05**

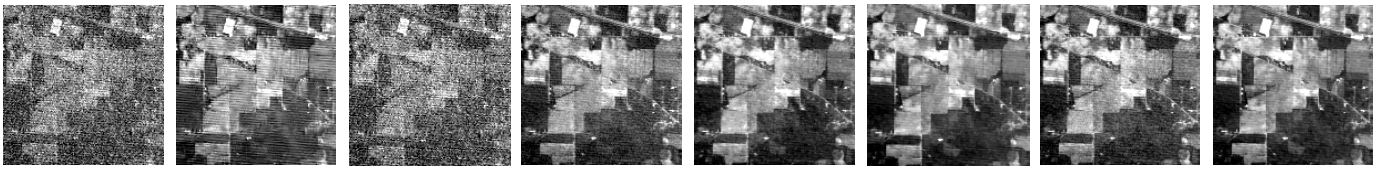

(a) (b) (c) (d) (e) (f) (g) (h)

Fig. 17. Indian Pines data set image after denoising. (a) Original image of band 1. The restored image of (b) BM4D, (c) TDL, (d) LRMR, (e) LRTV, (f) LSSTV, (g) LLRSSTV, and (h) TV-NLRTD.

(a) (b) (c) (d) (e) (f) (g) (h)

Fig. 18. Indian Pines data set image after denoising. (a) Original image of band 109. The restored images of (b) BM4D, (c) TDL, (d) LRMR, (e) LRTV, (f) LSSTV, (g) LLRSSTV, and (h) TV-NLRTD.

1) AVIRIS Indian Pines Data Set: The Indian Pines data set (available at: https://engineer-ing.purdue.edu/~biehl/MultiSpec/hyperspectral.html) was acquired by the NASA AVIRIS sensor and has a size of 145 × 145 × 220. As shown in Fig. 16(a), the data set is corrupted by dense noise, impulse noise, atmospheric effects, and water absorption.

Figs. 17 and 18 show the visual performance of the different methods for some typical bands. For the heavily contaminated HSI bands, such as band 1 and band 109, the TDL and BM4D methods perform unsatisfactorily in image restoration. The LRMR, LSSTV, and LLRSSTV methods achieve a better performance than these three methods but still leave a part of the mixed noise, such as the horizontal stripes shown in Fig. 17(d) and (g) and the Gaussian/impulse noise shown in Fig. 18(d) and (g). The LRTV method removes most of the noise, but, unfortunately, as shown in Figs. 17(e) and 18(e), the local details tend to be oversmoothed at the same time. From Figs. 17(h) and 18(h), it can be seen that the proposed TV-NLRTD method suppresses most of the noise effectively while preserving the image details at the same time, thus achieving the best visual results.

TABLE II
QUANTITATIVE EVALUATION RESULTS OF THE DIFFERENT DENOISING METHODS ON THE PAVIA CITY CENTER DATA SET

Noise case	Level	Evaluation index	Noise	BM4D	LRMR	TDL	LRTV	LSSTV	LLRSSTV	TV-NLRTD
Case 1	G=0.025 P=0.05	PSNR	17.41	28.42	40.90	31.72	41.63	40.47	43.21	**43.98**
		SSIM	0.451	0.837	0.987	0.932	0.982	0.977	0.991	**0.994**
		SAM	0.566	0.170	0.058	0.092	0.067	0.079	0.048	**0.045**
		ERGAS	501.25	197.98	34.21	96.34	67.40	73.33	25.98	**23.91**
	G=0.05 P=0.1	PSNR	14.28	25.24	36.81	27.30	37.97	36.82	38.55	**39.42**
		SSIM	0.246	0.702	0.969	0.868	0.966	0.969	0.975	**0.982**
		SAM	0.704	0.234	0.081	0.114	0.100	0.138	0.074	**0.063**
		ERGAS	718.60	207.30	54.87	160.81	100.97	120.22	44.52	**40.10**
	G=0.075 P=0.15	PSNR	12.40	24.28	33.72	24.07	35.36	34.41	35.18	**36.26**
		SSIM	0.153	0.681	0.941	0.783	0.946	0.947	0.951	**0.968**
		SAM	0.771	0.178	0.102	0.140	0.134	0.149	0.097	**0.077**
		ERGAS	888.45	227.11	77.61	233.21	121.14	132.25	62.25	**56.78**
	G=0.1 P=0.2	PSNR	11.09	22.45	31.57	21.85	32.08	32.37	32.53	**33.52**
		SSIM	0.105	0.617	0.908	0.707	0.909	0.919	0.920	**0.943**
		SAM	0.808	0.172	0.117	0.154	0.216	0.224	0.119	**0.098**
		ERGAS	1.035e+3	280.55	98.35	302.44	170.90	100.24	87.92	**78.42**
Case 2	Gaussian + impulse	PSNR	13.99	25.32	32.94	23.93	34.28	34.46	34.58	**35.97**
		SSIM	0.221	0.710	0.931	0.656	0.935	0.941	0.947	**0.964**
		SAM	0.742	0.192	0.113	0.244	0.230	0.204	0.155	**0.087**
		ERGAS	802.56	209.07	85.92	261.21	147.06	101.27	95.73	**62.15**
Case 3	Gaussian +stripes+ impulse	PSNR	13.78	25.01	32.41	23.38	34.03	34.33	33.83	**35.26**
		SSIM	0.210	0.697	0.926	0.617	0.932	0.941	0.937	**0.956**
		SAM	0.751	0.198	0.119	0.261	0.240	0.211	0.189	**0.115**
		ERGAS	813.79	215.13	90.76	274.60	152.32	114.61	111.66	**76.71**

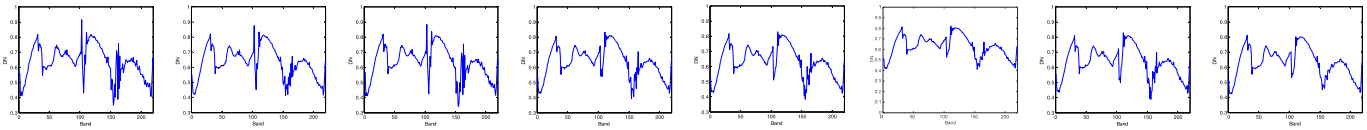

(a) (b) (c) (d) (e) (f) (g) (h)

Fig. 19. Spectrum of the pixel (80, 80) from the Indian Pines restoration results. (a) Original. (b) BM4D. (c) TDL. (d) LRMR. (e) LRTV. (f) LSSTV. (g) LLRSSTV. (h) TV-NLRTD.

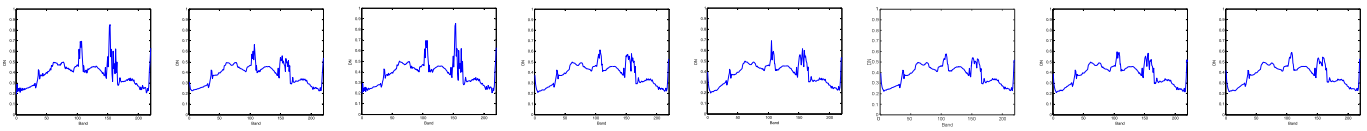

(a) (b) (c) (d) (e) (f) (g) (h)

Fig. 20. Spectrum of the pixel (30, 60) from the Indian Pines restoration results. (a) Original. (b) BM4D. (c) TDL. (d) LRMR. (e) LRTV. (f) LSSTV. (g) LLRSSTV. (h) TV-NLRTD.

For a more detailed comparison, the spectral signatures of some typical objects are presented in Figs. 19 and 20. The horizontal axis represents the number of spectral bands, and the vertical axis represents the DN values of Figs. 19 and 20.

According to the official description of the Indian Pines data set, pixel (80, 80) represents the "Corn-notill" class and pixel (30, 60) belongs to the "Grass-trees" class. In Figs. 19(b)–(d) and 20(b)–(d), the LRMR, TDL, and ITSReg methods cause evident jagged distortion in the recovered spectra, which indicates that these methods fail to remove the heavy noise. Clearly, it can be seen that the curve of the proposed TV-NLRTD method is much smoother than those of the other methods, which further illustrates that the proposed model is better able to maintain the spectral information.

2) HYDICE Urban Data Set: The Urban data set was acquired by the HYDICE sensor and has a size of 307 × 307 × 210. A subimage of size 200 × 200 × 210 was selected in this experiment. As shown in Fig. 16(b), this data set is contaminated with the Gaussian noise, deadlines, and stripes.

Figs. 21 and 22 present the denoising results for band 139 and band 206 of the Urban data set via the different methods. From Figs. 21 and 22, it can be observed that stripes, deadlines, and the Gaussian noise result in significant corruption of the Urban data set. It is clear that the nonlocal-based methods, i.e., BM4D and TDL, cannot effectively remove the mixed noise. Since the LRTV, LSSTV, and LLRSSTV methods utilize TV regularization, they can suppress this kind of noise, to some degree. By combining SSTV and the

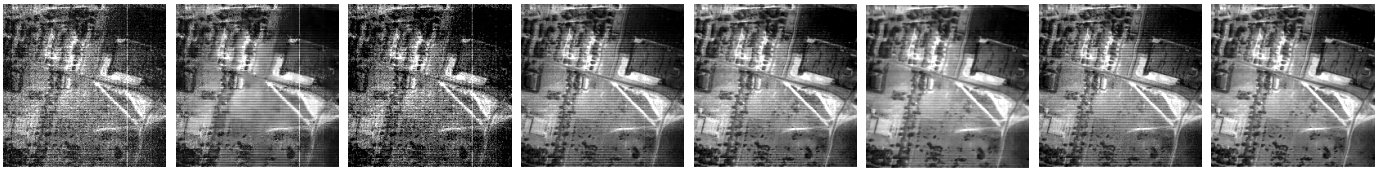

(a) (b) (c) (d) (e) (f) (g) (h)

Fig. 21. HYDICE Urban data set image after denoising. (a) Original image of band 139. The restored images of (b) BM4D, (c) TDL, (d) LRMR, (e) LRTV, (f) LSSTV, (g) LLRSSTV, and (h) TV-NLRTD.

(a) (b) (c) (d) (e) (f) (g) (h)

Fig. 22. HYDICE Urban data set image after denoising. (a) Original image of band 206. The restored images of (b) BM4D, (c) TDL, (d) LRMR, (e) LRTV, (f) LSSTV, (g) LLRSSTV, and (h) TV-NLRTD.

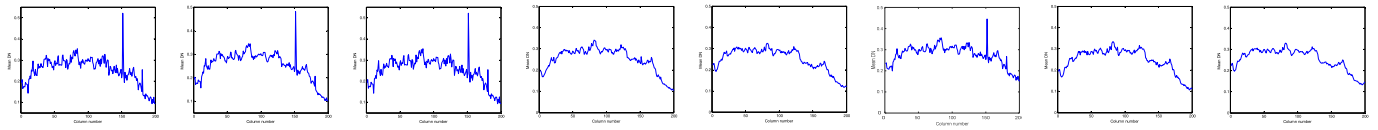

(a) (b) (c) (d) (e) (f) (g) (h)

Fig. 23. Vertical mean profiles of band 139 in the Urban image restoration experiment. (a) Original. (b) BM4D. (c) TDL. (d) LRMR. (e) LRTV. (f) LSSTV. (g) LLRSSTV. (h) TV-NLRTD.

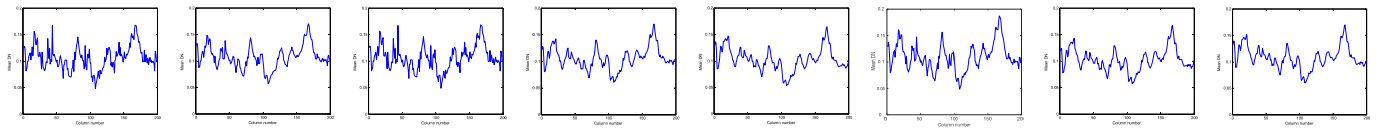

(a) (b) (c) (d) (e) (f) (g) (h)

Fig. 24. Vertical mean profiles of band 206 in the Urban image restoration experiment. (a) Original. (b) BM4D. (c) TDL. (d) LRMR. (e) LRTV. (f) LSSTV. (g) LLRSSTV. (h) TV-NLRTD.

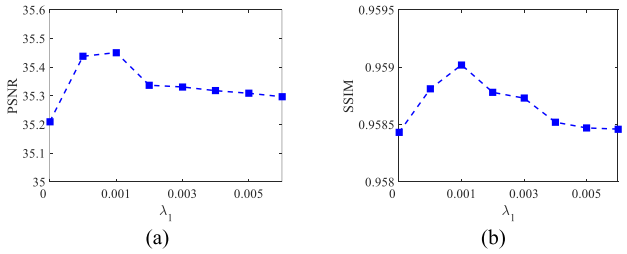

(a) (b)

Fig. 25. Denoising performance with different values of λ_1. (a) PSNR. (b) SSIM.

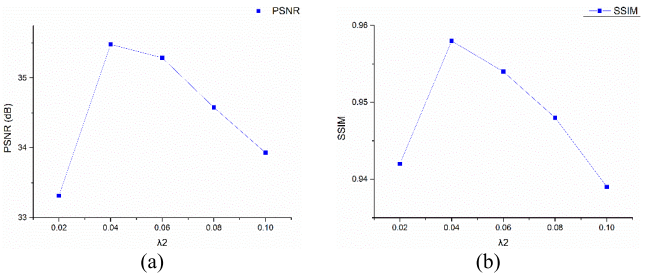

(a) (b)

Fig. 26. Denoising performances with different values of λ_2. (a) PSNR. (b) SSIM.

nonlocal low-rank decomposition, the proposed TV-NLRTD method can eliminate the mixed noise to the greatest extent while preserving the image details.

The vertical mean profiles of band 139 and band 206 are presented in Figs. 23 and 24 to allow a more intuitive verification of the denoising performance. The vertical axis represents the DN value, and the horizontal axis represents the column number in Figs. 23 and 24. The rapid fluctuation in Figs. 23(a) and 24(a) indicates the existence of sparse noise. From Figs. 23(a) and 24(a), it can be seen that only the LRMR, LRTV, LSSTV, LLRSSTV, and TV-NLRTD methods can remove the stripes in the vertical direction, thus verifying the conclusion made from the visual effects. However, the proposed TV-NLRTD method provides a smoother curve in the vertical direction, indicating that the stripes and other types of noise have been eliminated more effectively.

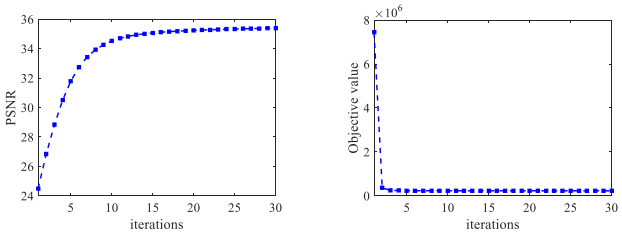

Fig. 27. Denoising performance with the iterations. (a) PSNR. (b) Objective values defined by (12).

TABLE III

RUN TIMES (IN SECONDS) OF THE DIFFERENT METHODS IN THE REAL DATA EXPERIMENTS

Method	BM4D	LRMR	TDL	LRTV	LSSTV	LLR-SSTV	TV-NLRTD
Indian	261	198	42	408	62	125	155
Urban	452	417	102	679	106	208	366

C. Discussion

1) Parameter Analysis: In the TV-NLRTD method, the denoising performance is influenced by the values of the regularization parameters and the block size for the nonlocal similarity searching. In the optimization procedure, parameter λ_3 represents the balance between the nonlocal low-rank item and the global data fidelity item in the whole model. We fixed λ_3 as 1, as in [48]. Thus, in this section, we only discuss the SSTV regularization parameter λ_1 and the sparse noise regularization parameter λ_2.

Parameter λ_1 balances the weight of the global SSTV regularization. By fixing λ_2 as the optimum value, we adjusted λ_1 within the scope of [0, 0.006]. PSNR and SSIM values versus parameter λ_1 are presented in Fig. 25 for the simulated Pavia data set in noise in Case 3. Clearly, the denoising performance is relatively robust to parameter λ_1. For the simulated and real data experiments, λ_1 was set to 0.001.

Parameter λ_2 restrains the sparsity of the sparse noise. First, parameter λ_1 was fixed as the optimum value, and we then changed parameter λ_2 from 0.02 to 0.1 with a step size of 0.02. Fig. 26 shows the PSNR and SSIM values versus parameter λ_2, where it can be observed that the increase in performance is very fast with the growth of λ_2 and reaches a peak when it reaches 0.04. The performance then gradually declines. This demonstrates that parameter λ_2 is relatively stable within a certain range. Parameter λ_2 was set to 0.04 in all the experiments, for a good denoising performance.

2) Convergence Illustration: To illustrate the convergence of TV-NLRTD, the PSNR and the objective values (12) of each iteration for the simulated Pavia data set in Case 2 are presented in Fig. 27. As shown in Fig. 27, it is clear that the relative changes in PSNR and the objective values are gradual as the iterative process takes place, which demonstrates that the proposed TV-NLRTD method can converge to a good local solution.

3) Time Cost: We conducted all the experiments in MATLAB 2014a with an Intel i7 CPU at 2.60 GHz and 12 GB of memory. Table III presents the time cost of the different methods for the two real data sets. From Table III, it can be observed that the proposed method is competitive compared to the other state-of-the-art methods.

V. CONCLUSION

In this article, we have proposed a novel SSTV TV-NLRTD method for the removal of mixed noise in hyperspectral imagery. With the nonlocal similarity of the HSI cube, a nonlocal low-rank tensor decomposition model is built to explore the low-rank property of the similar HSI 3-D cubes. SSTV regularization is then further integrated to exploit the local piecewise smoothness of the clean HSI. Finally, the efficient ADMM algorithm is utilized to solve the resulting TV-NLRTD method. Two simulated data experiments and two real data experiments were conducted to illustrate the effectiveness of the proposed TV-NLRTD method. The experimental results confirmed that the proposed TV-NLRTD method achieves a superior denoising performance, from both the visual and quantitative evaluations.

Nevertheless, there is still room for improvement of the proposed TV-NLRTD algorithm. As the noise intensity of different HSI bands varies greatly, a weighting strategy will be considered by assigning different weights for each band, according to the noise intensity. In addition, the adaptive determination of the regularization parameters will be addressed in our future work.

ACKNOWLEDGMENT

The authors would like to thank the Editor and the anonymous reviewers, who gave valuable comments and helped to improve the quality of this article.

REFERENCES

[1] J. M. Bioucas-Dias, A. Plaza, G. Camps-Valls, P. Scheunders, N. M. Nasrabadi, and J. Chanussot, "Hyperspectral remote sensing data analysis and future challenges," *IEEE Geosci. Remote Sens. Mag.*, vol. 1, no. 2, pp. 6–36, Jun. 2013.

[2] D. Haboudane, J. Miller, E. Pattey, P. J. Zarco-Tejada, and I. Strachan, "Hyperspectral vegetation indices and novel algorithms for predicting green LAI of crop canopies: Modeling and validation in the context of precision agriculture," *Remote Sens. Environ.*, vol. 90, no. 3, pp. 337–352, Apr. 2004.

[3] F. A. Kruse, J. W. Boardman, and J. F. Huntington, "Comparison of airborne hyperspectral data and EO-1 Hyperion for mineral mapping," *IEEE Trans. Geosci. Remote Sens.*, vol. 41, no. 6, pp. 1388–1400, Jun. 2003.

[4] J. M. Bioucas-Dias *et al.*, "Hyperspectral unmixing overview: Geometrical, statistical, and sparse regression-based approaches," *IEEE J. Sel. Topics Appl. Earth Observ. Remote Sens.*, vol. 5, no. 2, pp. 354–379, Apr. 2012.

[5] T. G. Kolda and B. W. Bader, "Tensor decompositions and applications," *SIAM Rev.*, vol. 51, no. 3, pp. 455–500, 2009.

[6] B. Rasti, J. R. Sveinsson, M. O. Ulfarsson, and J. A. Benediktsson, "Hyperspectral image denoising using first order spectral roughness penalty in wavelet domain," *IEEE J. Sel. Topics Appl. Earth Observ. Remote Sens.*, vol. 7, no. 6, pp. 2458–2467, Jun. 2014.

[7] S.-L. Chen, X.-Y. Hu, and S.-L. Peng, "Hyperspectral imagery denoising using a spatial-spectral domain mixing prior," *J. Comput. Sci. Technol.*, vol. 27, no. 4, pp. 851–861, Jul. 2012.

[8] M. Elad and M. Aharon, "Image denoising via sparse and redundant representations over learned dictionaries," *IEEE Trans. Image Process.*, vol. 15, no. 12, pp. 3736–3745, Dec. 2006.

[9] K. Dabov, A. Foi, V. Katkovnik, and K. Egiazarian, "Image denoising by sparse 3-D transform-domain collaborative filtering," *IEEE Trans. Image Process.*, vol. 16, no. 8, pp. 2080–2095, Aug. 2007.

[10] D. Letexier and S. Bourennane, "Noise removal from hyperspectral images by multidimensional filtering," *IEEE Trans. Geosci. Remote Sens.*, vol. 46, no. 7, pp. 2061–2069, Jul. 2008.

[11] W. He, N. Yokoya, L. Yuan, and Q. Zhao, "Remote sensing image reconstruction using tensor ring completion and total variation," *IEEE Trans. Geosci. Remote Sens.*, to be published. doi: 10.1109/TGRS.2019.2924017.

[12] F. Xu, X. Bai, and J. Zhou, "Non-local similarity based tensor decomposition for hyperspectral image denoising," in *Proc. IEEE Int. Conf. Image Process. (ICIP)*, Beijing, China, Sep. 2017, pp. 1890–1894.

[13] Y. W. Wen, M. K. Ng, and Y. M. Huang, "Efficient total variation minimization methods for color image restoration," *IEEE Trans. Image Process.*, vol. 17, no. 11, pp. 2081–2088, Nov. 2008.

[14] A. Buades, B. Coll, and J.-M. Morel, "A non-local algorithm for image denoising," in *Proc. IEEE Comput. Soc. Conf. Comput. Vis. Pattern Recognit. (CVPR)*, Jun. 2005, pp. 60–65.

[15] A. Chopra and H. Lian, "Total variation, adaptive total variation and nonconvex smoothly clipped absolute deviation penalty for denoising blocky images," *Pattern Recognit.*, vol. 43, no. 8, pp. 2609–2619, 2010.

[16] M. Jung, X. Bresson, T. F. Chan, and L. A. Vese, "Nonlocal Mumford–Shah regularizers for color image restoration," *IEEE Trans. Image Process.*, vol. 20, no. 6, pp. 1583–1598, Jun. 2011.

[17] J. Wright, A. Ganesh, S. Rao, Y. Peng, and Y. Ma, "Robust principal component analysis: Exact recovery of corrupted low-rank matrices via convex optimization," in *Proc. Adv. Neural Inf. Process. Syst.*, 2009, pp. 2080–2088.

[18] H. Zhai, H. Zhang, L. Zhang, and P. Li, "Total variation regularized collaborative representation clustering with a locally adaptive dictionary for hyperspectral imagery," *IEEE Trans. Geosci. Remote Sens.*, vol. 57, no. 1, pp. 166–180, Jan. 2019.

[19] W. Dong, L. Zhang, G. Shi, and X. Li, "Nonlocally centralized sparse representation for image restoration," *IEEE Trans. Image Process.*, vol. 22, no. 4, pp. 1620–1630, Apr. 2013.

[20] J. Li, Q. Yuan, H. Shen, and L. Zhang, "Hyperspectral image recovery employing a multidimensional nonlocal total variation model," *Signal Process.*, vol. 111, pp. 230–248, Jun. 2015.

[21] R. Courant, "Variational methods for the solution of problems of equilibrium and vibration," *Bull. Amer. Math. Soc.*, vol. 49, pp. 1–23, Jul. 1943.

[22] Y. Chang, L. Yan, H. Fang, and H. Liu, "Simultaneous destriping and denoising for remote sensing images with unidirectional total variation and sparse representation," *IEEE Geosci. Remote Sens. Lett.*, vol. 11, no. 6, pp. 1051–1055, Jun. 2014.

[23] Y. Chang, L. Yan, H. Fang, and C. Luo, "Anisotropic spectral-spatial total variation model for multispectral remote sensing image destriping," *IEEE Trans. Image Process.*, vol. 24, no. 6, pp. 1852–1866, Jun. 2015.

[24] M.-D. Iordache, J. Bioucas-Dias, and A. Plaza, "Total variation spatial regularization for sparse hyperspectral unmixing," *IEEE Trans. Geosci. Remote Sens.*, vol. 50, no. 11, pp. 4484–4502, Nov. 2012.

[25] T.-X. Jiang, L. Zhuang, T.-Z. Huang, and J. M. Bioucas-Dias, "Adaptive hyperspectral mixed noise removal," in *Proc. IEEE Int. Geosci. Remote Sens. Symp.*, Jul. 2018, pp. 4035–4038.

[26] Y. Chen, T.-Z. Huang, and X.-L. Zhao, "Destriping of multispectral remote sensing image using low-rank tensor decomposition," *IEEE J. Sel. Topics Appl. Earth Observ. Remote Sens.*, vol. 11, no. 12, pp. 4950–4967, Dec. 2018.

[27] H. Zhang, W. He, L. Zhang, H. Shen, and Q. Yuan, "Hyperspectral image restoration using low-rank matrix recovery," *IEEE Trans. Geosci. Remote Sens.*, vol. 52, no. 8, pp. 4729–4743, Aug. 2014.

[28] F. Fan, Y. Ma, C. Li, X. Mei, J. Huang, and J. Ma, "Hyperspectral image denoising with superpixel segmentation and low-rank representation," *Inf. Sci.*, vol. 58, no. 3, pp. 48–68, Aug. 2017.

[29] M. Wang, J. Yu, J.-H. Xue, and W. Sun, "Denoising of hyperspectral images using group low-rank representation," *IEEE J. Sel. Topics Appl. Earth Observ. Remote Sens.*, vol. 9, no. 9, pp. 4420–4427, Sep. 2016.

[30] W. He, H. Zhang, and L. Zhang, "Total variation regularized reweighted sparse nonnegative matrix factorization for hyperspectral unmixing," *IEEE Trans. Geosci. Remote Sens.*, vol. 55, no. 7, pp. 3909–3921, Jul. 2017.

[31] W. He, H. Zhang, L. Zhang, and H. Shen, "Total-variation-regularized low-rank matrix factorization for hyperspectral image restoration," *IEEE Trans. Geosci. Remote Sens.*, vol. 54, no. 1, pp. 178–188, Jan. 2016.

[32] S. Boyd, N. Parikh, E. Chu, B. Peleato, and J. Eckstein, "Distributed optimization and statistical learning via the alternating direction method of multipliers," *Found. Trends Mach. Learn.*, vol. 3, no. 1, pp. 1–122, Jan. 2011.

[33] J. D. Carroll and J.-J. Chang, "Analysis of individual differences in multidimensional scaling via an n-way generalization of 'Eckart-Young' decomposition," *Psychometrika*, vol. 35, no. 3, pp. 283–319, Sep. 1970.

[34] R. A. Harshman, "Foundations of the PARAFAC procedure: Models and conditions for an, 'explanatory' multi-modal factor analysis," *UCLA Work. Papers Phonetics*, vol. 16, no. 1, pp. 1–84, 1970.

[35] A. H. Kiers, "Towards a standardized notation and terminology in multiway analysis," *J. Chemometrics*, vol. 14, no. 3, pp. 105–122, 2000.

[36] L. R. Tucker, "Some mathematical notes on three-mode factor analysis," *Psychometrika*, vol. 31, no. 3, pp. 279–311, 1966.

[37] Y. Chen, W. He, N. Yokoya, and T.-Z. Huang, "Hyperspectral image restoration using weighted group sparsity-regularized low-rank tensor decomposition," *IEEE Trans. Cybern.*, to be published. doi: 10.1109/TCYB.2019.2936042.

[38] D. Muti and S. Bourennane, "Multidimensional filtering based on a tensor approach," *Signal Process.*, vol. 85, no. 12, pp. 2338–2353, 2005.

[39] W. Cao *et al.*, "Total variation regularized tensor RPCA for background subtraction from compressive measurements," *IEEE Trans. Image Process.*, vol. 25, no. 9, pp. 4075–4090, Sep. 2016.

[40] Q. Wang, Z. Wu, J. Jin, T. Wang, and Y. Shen, "Low rank constraint and spatial spectral total variation for hyperspectral image mixed denoising," *Signal Process.*, vol. 142, pp. 11–26, Jan. 2018.

[41] H. Fan, Y. Chen, Y. Guo, H. Zhang, and G. Kuang, "Hyperspectral image restoration using low-rank tensor recovery," *IEEE J. Sel. Topics Appl. Earth Observ. Remote Sens.*, vol. 10, no. 10, pp. 4589–4604, Oct. 2017.

[42] D. Arthur and S. Vassilvitskii, "k-means++: The advantages of careful seeding," in *Proc. ACM-SIAM Symp. Discrete Algorithms*, Philadelphia, PA, USA, Jan. 2007, pp. 1027–1035.

[43] J. Li, H. Shen, Q. Yuan, L. Zhang, and W. Gong, "Hypspectral image denoising via multidimensional nonlocal model," in *Proc. 5th Workshop Hyperspectral Image Signal Process., Evol. Remote Sens. (WHISPERS)*, Jun. 2013, pp. 1–4.

[44] S. H. Chan, R. Khoshabeh, K. B. Gibson, P. E. Gill, and T. Q. Nguyen, "An augmented Lagrangian method for total variation video restoration," *IEEE Trans. Image Process.*, vol. 20, no. 11, pp. 3097–3111, Nov. 2011.

[45] G. Liu, Z. Lin, S. Yan, J. Sun, Y. Yu, and Y. Ma, "Robust recovery of subspace structures by low-rank representation," *IEEE Trans. Pattern Anal. Mach. Intell.*, vol. 35, no. 1, pp. 171–184, Jan. 2013.

[46] M. Maggioni, V. Katkovnik, K. Egiazarian, and A. Foi, "Nonlocal transform-domain filter for volumetric data denoising and reconstruction," *IEEE Trans. Image Process.*, vol. 22, no. 1, pp. 33–119, Jan. 2012.

[47] Y. Peng, D. Meng, Z. Xu, C. Gao, Y. Yang, and B. Zhang, "Decomposable nonlocal tensor dictionary learning for multispectral image denoising," in *Proc. IEEE Conf. Comput. Vis. Pattern Recognit.*, Jun. 2014, pp. 2949–2956.

[48] Y. Chang, L. Yan, and S. Zhong, "Hyper-Laplacian regularized unidirectional low-rank tensor recovery for multispectral image denoising," in *Proc. IEEE Conf. Comput. Vis. Pattern Recognit. (CVPR)*, Jul. 2017, pp. 4260–4268.

[49] H. Zhang, "Hyperspectral image denoising with cubic total variation model," *SPRS Ann. Photogramm., Remote Sens. Spatial Inf. Sci.*, vol. 7, pp. 95–98, Jul. 2012.

[50] Q. Xie *et al.*, "Multispectral images denoising by intrinsic tensor sparsity regularization," in *Proc. IEEE Conf. Comput. Vis. Pattern Recognit. (CVPR)*, Jun. 2016, pp. 1692–1700.

[51] W. He, H. Zhang, H. Shen, and L. Zhang, "Hyperspectral image denoising using local low-rank matrix recovery and global spatial–spectral total variation," *IEEE J. Sel. Topics Appl. Earth Observ. Remote Sens.*, vol. 11, no. 3, pp. 713–729, Mar. 2018.

[52] Z. Wang, A. C. Bovik, H. R. Sheikh, and E. P. Simoncelli, "Image quality assessment: From error visibility to structural similarity," *IEEE Trans. Image Process.*, vol. 13, no. 4, pp. 600–612, Apr. 2004.

[53] L. Wald, *Data Fusion: Definitions and Architectures: Fusion of Images of Different Spatial Resolutions*. France, Paris: Les Presses de l'Ecole des Mines, 2002.

[54] R. O. Green, "Discrimination among semi-arid landscape endmembers using the spectral angle mapper (SAM) algorithm," in *Proc. 3rd Annu. JPL Airborne Geosci. Workshop*, vol. 1, 1992, pp. 147–149.

[55] D. Muti, S. Bourennane, and J. Marot, "Lower-rank tensor approximation and multiway filtering," *SIAM J. Matrix Anal. Appl.*, vol. 30, no. 3, pp. 1172–1204, 2008.

[56] Y. Wang, J. Peng, Q. Zhao, D. Meng, Y. Leung, and X.-L. Zhao, "Hyperspectral image restoration via total variation regularized low-rank tensor decomposition," *IEEE J. Sel. Topics Appl. Earth Observ. Remote Sens.*, vol. 11, no. 4, pp. 1227–1243, Apr. 2018.

[57] G. Chen and S.-E. Qian, "Denoising of hyperspectral imagery using principal component analysis and wavelet shrinkage," *IEEE Trans. Geosci. Remote Sens.*, vol. 49, no. 3, pp. 973–980, Mar. 2014.
[58] X. Bai, F. Xu, L. Zhou, Y. Xing, L. Bai, and J. Zhou, "Nonlocal similarity based nonnegative tucker decomposition for hyperspectral image denoising," *IEEE J. Sel. Topics Appl. Earth Observ. Remote Sens.*, vol. 11, no. 3, pp. 701–712, Mar. 2018.
[59] J. Xue and Y. Zhao, "Rank-1 tensor decomposition for hyperspectral image denoising with non-local low-rank regularization," in *Proc. Int. Conf. Mach. Vis. Inf. Technol. (CMVIT)*, Singapore, Feb. 2017, pp. 40–45.
[60] H. Zhai, H. Zhang, L. Zhang, and P. Li, "Laplacian-regularized low-rank subspace clustering for hyperspectral image band selection," *IEEE Trans. Geosci. Remote Sens.*, vol. 57, no. 3, pp. 1723–1740, Mar. 2019.
[61] *Pavia City Center*. (2019). [Online]. Available: http://www.ehu.es/ccwintco/index.php/Hyperspectral_Remote_Sensing_Scenes

Hongyan Zhang (M'13–SM'16) received the B.S. degree in geographic information system and the Ph.D. degree in photogrammetry and remote sensing from Wuhan University, Wuhan, China, in 2005 and 2010, respectively.

Since 2016, he has been a Full Professor with the State Key Laboratory of Information Engineering in Surveying, Mapping, and Remote Sensing, Wuhan University. He is currently a Young Chang-Jiang Scholar appointed by the Ministry of Education of China. He has authored/coauthored more than 90 research articles and 5 talents. His research interests include image reconstruction for quality improvement, hyperspectral information processing, and agricultural remote sensing.

Dr. Zhang scored first in the Pairwise Semantic Stereo Challenge of the 2019 Data Fusion Contest organized by the IEEE Image Analysis and Data Fusion Technical Committee. He serves as an Associate Editor for *Photogrammetric Engineering & Remote Sensing* and *Computers & Geosciences* and the Session Chair for the 2016 IEEE IGARSS conference and the 2015 IEEE WHISPERS conference. He is a Reviewer of more than 30 international academic journals, including the IEEE TRANSACTIONS ON GEOSCIENCE AND REMOTE SENSING, the IEEE TRANSACTIONS ON IMAGE PROCESSING, the IEEE JOURNAL OF SELECTED TOPICS IN APPLIED EARTH OBSERVATIONS AND REMOTE SENSING, and the IEEE GEOSCIENCE AND REMOTE SENSING LETTERS.

Lu Liu received the B.S. degree from the College of Information Science and Engineering, Shandong Agricultural University, Tai'an, China, in 2012. She is currently pursuing the M.S. degree with the State Key Laboratory of Information Engineering in Surveying, Mapping, and Remote Sensing, Wuhan University, Wuhan, China.

Her research interests include compressive sensing and hyperspectral image denoising.

Wei He (S'14–M'17) received the B.S. degree from the School of Mathematics and Statistics and the Ph.D. degree from the State Key Laboratory of Information Engineering in Surveying, Mapping, and Remote Sensing, Wuhan University, Wuhan, China, in 2012 and 2017, respectively.

He is currently a Researcher with RIKEN Center for Advanced Intelligence Project, Geoinformatics Unit, Wako, Japan. His research interests include image quality improvement, remote sensing image processing, and low-rank representation.

Liangpei Zhang (M'06–SM'08–F'19) received the B.S. degree in physics from Hunan Normal University, Changsha, China, in 1982, the M.S. degree in optics from the Xi'an Institute of Optics and Precision Mechanics of the Chinese Academy of Sciences, Xi'an, China, in 1988, and the Ph.D. degree in photogrammetry and remote sensing from Wuhan University, Wuhan, China, in 1998.

He is currently the Head of the Remote Sensing Division, State Key Laboratory of Information Engineering in Surveying, Mapping, and Remote Sensing, Wuhan University. He is also the Chang-Jiang Scholar Chair Professor appointed by the Ministry of Education of China. He is also a Principal Scientist for the China State Key Basic Research Project (2011–2016) appointed by the Ministry of National Science and Technology of China to lead the remote sensing program in China. He has published more than 500 research articles and five books. He holds 15 patents. His research interests include hyperspectral remote sensing, high-resolution remote sensing, image processing, and artificial intelligence.

Dr. Zhang is a Fellow of the Institution of Engineering and Technology and an Executive Member (Board of Governors) of the China National Committee of the International Geosphere–Biosphere Program and the China Society of Image and Graphics. He was a recipient of the 2010 Best Paper Boeing Award, the 2013 Best Paper ERDAS Award of the American Society of Photogrammetry and Remote Sensing (ASPRS), and the Best Reviewer Award from the IEEE Geoscience and Remote Sensing Society (GRSS) for his service to the IEEE JOURNAL OF SELECTED TOPICS IN APPLIED EARTH OBSERVATIONS AND REMOTE SENSING (JSTARS) in 2012 and the IEEE GEOSCIENCE AND REMOTE SENSING LETTERS in 2014. His research teams received the top three prizes of the IEEE GRSS 2014 Data Fusion Contest, and his students have been selected as the winners or finalists of the IEEE International Geoscience and Remote Sensing Symposium Student Paper Contest in recent years. He is the Founding Chair of the IEEE GRSS, Wuhan Chapter. He regularly serves as the Co-Chair of the series of International Society for Optics and Photonics (SPIE) Conferences on Multispectral Image Processing and Pattern Recognition, the Conference on Asia Remote Sensing, and many other conferences. He was the General Chair of the Fourth IEEE GRSS Workshop on Hyperspectral Image and Signal Processing: Evolution in Remote Sensing (WHISPERS) and a Guest Editor of the IEEE JSTARS. He has served as Editor for several conference proceedings, issues, and geoinformatics symposiums. He also serves as an Associate Editor for the *International Journal of Ambient Computing and Intelligence*, the *International Journal of Image and Graphics*, the *International Journal of Digital Multimedia Broadcasting*, the *Journal of Geo-Spatial Information Science*, the *Journal of Remote Sensing*, and the IEEE TRANSACTIONS ON GEOSCIENCE AND REMOTE SENSING. He is a Guest Editor of the *Journal of Applied Remote Sensing* and the *Journal of Sensors*.